

## NEAR-INFRARED SPECTROSCOPY OF NITROGENATED POLYCYCLIC AROMATIC HYDROCARBON CATIONS FROM 0.7 TO 2.5 $\mu\text{m}$

ANDREW L. MATTIODA,<sup>1,2</sup> LINDSAY RUTTER,<sup>1,2,3</sup> JOHN PARKHILL,<sup>4</sup> MARTIN HEAD-GORDON,<sup>4</sup>  
TIMOTHY J. LEE,<sup>1</sup> AND LOUIS J. ALLAMANDOLA<sup>1</sup>

Received 2007 April 25; accepted 2007 December 21

### ABSTRACT

The near-infrared (NIR) spectra and absolute band strengths of 10 nitrogenated polycyclic aromatic hydrocarbon (PANH) radical cations isolated in an argon matrix are presented and compared with the spectra of their parent polycyclic aromatic hydrocarbon (PAH) radical cations. The 0.7–2.5  $\mu\text{m}$  (14,500–4000  $\text{cm}^{-1}$ ) spectrum for the open-shell cation forms of two nitrogenated anthracenes ( $\text{C}_{13}\text{H}_9\text{N}$  and  $\text{C}_{12}\text{H}_8\text{N}_2$ ), four isomeric nitrogenated benzanthracenes ( $\text{C}_{17}\text{H}_{11}\text{N}$ ), and four isomeric nitrogenated dibenzanthracenes ( $\text{C}_{21}\text{H}_{13}\text{N}$ ) are reported. These ionized PANHs have allowed electronic transitions that give rise to strong absorption bands in the NIR. Low-lying excited states for these PANH ions are computed using time-dependent density functional theory (TDDFT). The resulting vertical excitation spectrum characterizes the transitions, and leads to a simple model that predicts the qualitative trends in absorption energy. The direction of the shift depends on the position of the nitrogen atom within the PANH and the relative magnitudes of the donor and acceptor molecular orbitals involved in the transitions. As with non-nitrogenated PAHs, ionized interstellar PANHs can be expected to contribute to the mid-IR emission features from UV-rich as well as UV-poor regions, and add weak, broad band structure to the NIR region of the interstellar extinction curve.

*Subject headings:* astrochemistry — dust, extinction — ISM: general — ISM: molecules — molecular data

### 1. INTRODUCTION

More than 25 years of observations, theoretical development, and laboratory studies have led to the consensus that the mid-infrared (mid-IR) interstellar emission features, formerly referred to as the unidentified infrared (UIR) bands, are produced by mixtures of highly vibrationally excited polycyclic aromatic hydrocarbons (PAHs), PAH ions, and related species, including species such as PAH clusters and polycyclic aromatic nitrogen heterocycles, or PANHs. Detected in many galactic and extragalactic objects, including several with significant redshift, the interstellar infrared emission features present an important and unique probe of chemical and physical conditions across the universe. Recent reviews of the observational and laboratory work (e.g., Peeters et al. 2004; Hudgins & Allamandola 2004; Van Dishoeck 2004) and theoretical models (Verstraete et al. 2001; Bakes et al. 2001; Draine & Li 2001; Li & Draine 2001; Pech et al. 2002) can be found elsewhere.

Variations in the intensities, band profiles, and positions of the infrared emission provide important information about the nature of the emitting PAH population and reflect conditions in the emitting regions. The small shift in the peak position of the interstellar emission band near 6.2  $\mu\text{m}$  is one such variation. It was recognized that this could not be completely accommodated by the changes in the C-C stretching frequency of pure PAHs several years ago. However, the strong correlation of the 6.2  $\mu\text{m}$  feature with the other emission features assigned to PAHs indicated that these variations in peak position arose from small changes in the population of aromatic materials that were re-

sponsible for the emission band family. The constraints of cosmic abundance, chemical rules for aromaticity, and the proposed PAH circumstellar formation mechanisms are indications that the interstellar PAH population could include species in which a few nitrogen atoms are substituted for some of the carbon atoms that make up the molecule's fused hexagonal ring skeleton (Peeters et al. 2002; Hudgins et al. 2005). To test and refine this idea, Mattioda et al. (2003, 2005a) measured the mid-IR spectra of a number of two, three, and four-ring polycyclic aromatic nitrogen heterocycles (PANHs) and their cations, while Hudgins et al. (2005) theoretically determined the mid-IR spectra of larger, more complex, experimentally inaccessible PANHs. Taken together, these studies showed that PANHs readily accommodate the observed variations in the peak position of the strong interstellar emission feature near 6.2  $\mu\text{m}$  and make the case that the precise peak position is a measure of PANH size and nitrogen substitution pattern.

As part of our laboratory program to provide the overall spectroscopic properties of PAHs under interstellar conditions, Mattioda et al. (2005b) reported the near-infrared (NIR) spectra and absolute band strengths of 27 PAH cations ranging in size from  $\text{C}_{14}\text{H}_{10}$  to  $\text{C}_{50}\text{H}_{22}$ . This work was motivated in part by a desire to understand whether open-shell PAHs in UV poor radiation fields could be pumped into highly vibrationally excited states by NIR photons. Mattioda et al. (2005c) showed that this is indeed possible, and demonstrated that PAHs could be vibrationally excited even by the radiation from an M type star. With these data, Mattioda et al. (2005c) developed a semiempirical extension of the Li & Draine (2001, 2002) PAH UV-visible model spectrum through the NIR spectral range.

Here this NIR study is extended to include PANHs. The 0.7–2.5  $\mu\text{m}$  (14,500–4000  $\text{cm}^{-1}$ ) spectrum for the 10 PANHs and the three parent PAHs listed in Table 1 have been measured. These include anthracene ( $\text{C}_{14}\text{H}_{10}$ ) and two nitrogenated anthracenes, acridine ( $\text{C}_{13}\text{H}_9\text{N}$ ) and phenazine ( $\text{C}_{12}\text{H}_8\text{N}_2$ ); benz[*a*]anthracene

<sup>1</sup> NASA Ames Research Center, Moffett Field, CA 94035-1000; Andrew.L.Mattioda@nasa.gov.

<sup>2</sup> Carl Sagan Center, SETI Institute, 515 North Whisman Road, Mountain View, CA 94043.

<sup>3</sup> The Pennsylvania State University, University Park, PA 16802.

<sup>4</sup> University of California, Berkeley, CA 94720.

TABLE I  
NAME, FORMULA, STRUCTURE, AND RELATED EXPERIMENTAL INFORMATION FOR THE PANHs INVESTIGATED HERE

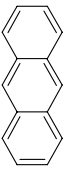
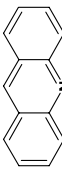
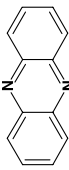
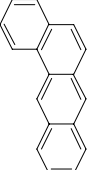
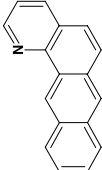
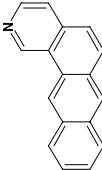
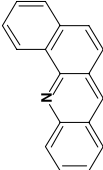
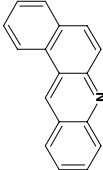
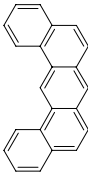
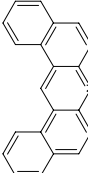
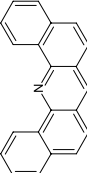
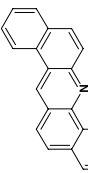
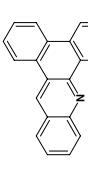
COMPOUND NAME	MOLECULAR FORMULA	CHEMICAL STRUCTURE	DEP. TEMP. (°C)	BAND CENTER (cm <sup>-1</sup> )		$\mu\text{m}$	$A$ km/mol ( $\times 10^3$ )	OSCILLATOR STRENGTH $f$		COMMENTS
				Theor.	Exp.			Exp. $\times 10^{-3}$	Theor. $\times 10^{-3}$	
anthracene	C <sub>14</sub> H <sub>10</sub>		50	15880	13835	0.723	48.2	9.01	108	Small features at 11620, 11190, 10864, 10460, 10165, 9520, 8353, 5956
acridine	C <sub>13</sub> H <sub>9</sub> N		25	13444	11306	0.884	31.9	5.97	108	Shoulder 12605, small feature at 9625
phenazine	C <sub>12</sub> H <sub>8</sub> N <sub>2</sub>		50	11581	9520	1.050	16.8	3.14	97.0	
1,2-bezanthracene or benz[ <i>a</i> ]anthracene	C <sub>18</sub> H <sub>12</sub>		85	13369	11215 11857 12484 Total	0.892 0.843 0.801	78.4 14.7 23.4 116.0	21.8	106	
1-azabenz[ <i>a</i> ]anthracene	C <sub>17</sub> H <sub>11</sub> N		81	14207	12076 13391 Total	0.828 0.747	59.8 12.9 72.7	13.6	127	Small feature between 6700 and 9000
2-azabenz[ <i>a</i> ]anthracene	C <sub>17</sub> H <sub>11</sub> N		98	14701	12762	0.784	9.61	1.80	98.4	Small features at 12145, 10115, 9845, 9770
benz[ <i>a</i> ]acridine	C <sub>17</sub> H <sub>11</sub> N		67	11491	8910 10371 Total cation 12862 13372	1.122 0.964	25.7 4.39 30.1 1.67 0.231	5.64	116	Anion band Anion band
benz[ <i>c</i> ]acridine	C <sub>17</sub> H <sub>11</sub> N		65	11496	9250 10783 Total cation 13100	1.081 0.927	80.0 24.1 104.0 1.26	19.5	104	Anion band

TABLE 1—Continued

COMPOUND NAME	MOLECULAR FORMULA	CHEMICAL STRUCTURE	DEP. TEMP. (°C)	BAND CENTER (cm <sup>-1</sup> )		A km/mol (×10 <sup>3</sup> )	OSCILLATOR STRENGTH <i>f</i>		COMMENTS
				Theor.	Exp.		μm	Exp. ×10 <sup>-3</sup>	
Dibenz[ <i>a,j</i> ]anthracene .....	C <sub>22</sub> H <sub>14</sub>		135	11964	9773	14.9	4.78	151	
					10188	4.05			
					10515	1.72			
					11252	4.92			
					Total cation	25.6			very small band at 8460; real??
dibenz[ <i>a,j</i> ]acridine .....	C <sub>21</sub> H <sub>13</sub> N		140	10262	7837	128.0	29.3	152	Side bands 8115, 8400
					9432	2.4			
					Total	156.0			
dibenz[ <i>c,h</i> ]acridine .....	C <sub>21</sub> H <sub>13</sub> N		110	10382	5844	1.53	38.6	138	
					8016	146.0			
					9878	60.1			
					Total w/o 5843	206.0			
dibenz[ <i>a,h</i> ]acridine .....	C <sub>21</sub> H <sub>13</sub> N		160	8724	7044	170.0	41.6	166	
					8635	52.7			
					Total	222.0			
dibenz[ <i>a,c</i> ]acridine .....	C <sub>21</sub> H <sub>13</sub> N		125	5840 12830	5219	5.83	12.8 3.72	47.3 70.9	
					6613	1.02			
					Total	6.85			
					11669	15.3			
					13097	4.57			
					Total	19.9			

(1,2 benzanthracene) ( $C_{18}H_{12}$ ) and four of the isomeric nitrogenated benzanthracenes, 1-azabenz[*a*]anthracene, 2-azabenz[*a*]anthracene, benz[*c*]acridine, and benz[*a*]acridine, all with formula  $C_{17}H_{11}N$ ; dibenz[*a,h*]anthracene ( $C_{22}H_{14}$ ) and four isomeric nitrogenated dibenzanthracenes, dibenz[*a,j*]acridine, dibenz[*c,h*]acridine, dibenz[*a,h*]acridine, and dibenz[*a,c*]acridine, all with formula  $C_{21}H_{13}N$ . As with PAHs, all the ionized PANHs we have studied have strong, broad absorption bands in the NIR arising from electronic transitions. The lowest lying electronic transitions for all of these species were computationally determined using time-dependent density functional theory (TDDFT) methods (Dreuw & Head-Gordon 2005), which are known to be generally reliable for PAH cations (Hirata et al. 2003). The computational spectra show that nitrogen plays an important role in determining the nature as well as the trends of the observed transitions. We conclude this paper by considering the role these PANH spectra play in pumping the mid-IR emission features and the weak, broadband structure they could superpose on the NIR portion of the interstellar extinction curve.

The work is presented as follows. The experimental and theoretical techniques are summarized in § 2, and the spectroscopic results are presented in § 3, where they are compared with related experimental and computational studies. Astrophysical considerations are discussed in § 4, and the conclusions are presented in § 5.

## 2. EXPERIMENTAL AND THEORETICAL METHODS

### 2.1. Experimental Methods

The matrix isolation infrared spectroscopy techniques employed in these studies have been described in detail previously (Hudgins & Allamandola 1995a; Hudgins & Sandford 1998) and will be summarized here only briefly. Matrix-isolated PANH samples were prepared by vapor codeposition of the species of interest with an overabundance of argon onto a 14 K CsI window suspended in a high-vacuum chamber ( $p < 10^{-7}$  Torr). The samples were vaporized from heated Pyrex tubes while argon was admitted through an adjacent length of copper tubing cooled by liquid nitrogen,  $N_2(l)$ . Deposition temperatures for the individual PANHs are provided in Table 1. Estimates based on the characteristic band intensities of PANHs and the calibrated argon deposition rate place the Ar/PANH ratio in these experiments in excess of 1000/1 (Mattioda et al. 2005a). The PANH samples utilized in this investigation were obtained from a variety of sources. Phenazine, 1-azabenz[*a*]anthracene, 2-azabenz[*a*]anthracene, and dibenz[*a,j*]anthracene samples were obtained from the National Cancer Institute's chemical Carcinogen Reference Standard Repository operated by the Midwest Research Institute and were of unspecified purity. Benz[*c*]acridine, benz[*a*]acridine, dibenz[*a,j*]acridine, dibenz[*c,h*]acridine, dibenz[*a,h*]acridine, and dibenz[*a,c*]acridine were obtained from the Chiron Chemical Company and have a purity greater than 99%. Acridine (97%), 1,2 benz[*a*]anthracene (99%), and anthracene (99%) were obtained from the Aldrich Chemical Company. Although the purity of the samples in this investigation varied, the absence of any notable discrepant mid-infrared spectral features between the theoretical and experimental spectra indicates that impurity levels are no more than a few percent (Mattioda et al. 2005a).

With the exception of benz[*a*]anthracene (Mattioda et al. 2005b), the near-infrared (NIR) spectra reported here were measured at  $2\text{ cm}^{-1}$  or higher resolution by co-adding 500 scans or more on a Digi Lab Excalibur 4000 Fourier transform infrared spectrometer. The spectra covered the  $15,000\text{--}3500\text{ cm}^{-1}$

( $0.66\text{--}2.86\text{ }\mu\text{m}$ ) range. Mid-infrared spectra ( $4000\text{--}500\text{ cm}^{-1}$ ,  $2.5\text{--}20\text{ }\mu\text{m}$ ) were measured for each of these samples as well, and will be reported elsewhere (A. L. Mattioda et al. 2008, in preparation). Spectra from  $15,000\text{--}9000\text{ cm}^{-1}$  ( $0.67\text{--}1.11\text{ }\mu\text{m}$ ) were collected using the spectrometer's NIR source (Tungsten lamp), quartz beam-splitter, and silicon detector. Using the same NIR source and quartz beam-splitter, PANH spectra between  $11,000$  and  $3500\text{ cm}^{-1}$  ( $0.91\text{--}2.86\text{ }\mu\text{m}$ ) were recorded by a liquid nitrogen cooled MCT-B detector. Spectra between  $7000$  and  $500\text{ cm}^{-1}$  ( $1.43\text{--}20\text{ }\mu\text{m}$ ) were collected using the same MCT-B detector in combination with a KBr beam-splitter and Globar source. The number of scans was chosen to optimize both the signal-to-noise ratio and time requirements of each experiment.

PANH ions were generated by in situ vacuum ultraviolet photolysis of the matrix-isolated neutral PANH compound. This was accomplished with the combined  $120\text{ nm Ly}\alpha$  ( $10.1\text{ eV}$ ) and the  $160\text{ nm}$  molecular hydrogen emission bands (centered around  $7.8\text{ eV}$ ) from a microwave powered discharge in a flowing  $H_2$  gas mixture at a dynamic pressure of  $150\text{ mTorr}$ . Comparison of the pre- and post-photolysis mid-infrared spectra permits identification of PANH ion features (e.g., Hudgins & Allamandola 1995b) and allows for the determination of the ionization percent of the sample (e.g., Mattioda et al. 2003). Assuming that all neutral PANH molecules that disappear are converted into ions, we can derive an upper limit to the ionization efficiency by measuring the percent decrease in the integrated areas of the neutral mid-infrared bands that accompany photolysis. Ionization efficiencies for PAHs are typically between 15% and 20%, but vary based on PAH size and structure. However, as noted in previous studies (Mattioda et al. 2003, 2005a), PANHs typically exhibit ionization efficiencies between 5% and 15%. In this investigation, the anthracene sample obtained a 10% ionization, acridine 8%, phenazine 6%, 1-azabenz[*a*]anthracene 19%, 2-azabenz[*a*]anthracene 6%, benz[*a*]acridine 5%, benz[*c*]acridine 6%, dibenz[*a,j*]anthracene 4%, dibenz[*a,j*]acridine 7%, dibenz[*c,h*]acridine 5%, and dibenz[*a,c*]acridine 9%. The results of benz[*a*]anthracene were taken from an earlier investigation (Mattioda et al. 2005b). To confirm the attribution of a photoproduct band, in both the mid and near-infrared spectrum, to the PANH cation, parallel experiments were conducted in which the argon matrix was doped with  $NO_2$ , an electron acceptor, at a concentration of approximately 1 part in 1200. The presence of this electron acceptor quenches the formation of anions and enhances the production of cations. As in our PAH NIR spectroscopic studies, we find that, in addition to cations, PANH anions are also produced in some cases. However, in the non-nitrogenated PAH study, anions were formed only for the aromatics containing more than 10 rings, and not for the smaller PAHs. This difference in behavior arises because the larger PAHs have electron affinities which are sufficiently high to capture and retain the photoelectrons under these experimental conditions, and this is not the case for the smaller PAHs. Interestingly, although the PANHs studied here are small, comprising no more than 5 rings, two (benz[*a*]acridine and benz[*c*]acridine) show evidence for some anion formation. The bands at  $12860$  and  $13370\text{ cm}^{-1}$  in benz[*a*]acridine and  $13100\text{ cm}^{-1}$  in benz[*c*]acridine (Fig. 2) are not present in the  $NO_2$  doped experiments. Computed adiabatic electron affinities (using the DFT methods discussed in § 2.2) are listed in Table 2. It is interesting to note that anion bands were detected in a previous mid-IR study of phenazine (Mattioda et al. 2005a), but this investigation revealed no NIR bands that could be attributed to anions.

The total number of PANH molecules was determined by taking the ratio of the sum of the experimental integrated band

TABLE 2  
COMPARISON OF THE CALCULATED AND EXPERIMENTAL ABSORPTION ENERGIES (eV)

Cation	Calculated Transition Energy (eV)	Experimental Transition Energy (eV)	$\langle S^2 \rangle$ (TDA)	Calculated Neutral Electron Affinity (eV)
anthracene .....	1.97	1.7154	0.7911	0.559
Acridine.....	1.67	1.4018	0.7922	0.892
phenazine .....	1.44	1.1803	0.7945	1.312
benz[ <i>a</i> ]anthracene .....	1.66	1.4701	0.783	0.599
1-azabenz[ <i>a</i> ]anthracene.....	1.76	1.4972	0.782	0.640
2-azabenz[ <i>a</i> ]anthracene.....	1.82	1.5823	0.788	0.860
benz[ <i>a</i> ]acridine.....	1.42	1.1047	0.7782	0.914
benz[ <i>a</i> ]acridine (anion).....	1.82	1.5947	0.7798	...
benz[ <i>a</i> ]acridine (anion).....	2.16	1.6579	0.7755	...
benz[ <i>c</i> ]acridine .....	1.43	1.1468	0.7737	0.880
benz[ <i>c</i> ]acridine (anion).....	1.85	1.6242	0.7796	...
dibenz[ <i>a,c</i> ]acridine.....	0.72	0.6471	0.7732	0.916
dibenz[ <i>a,j</i> ]anthracene.....	1.48	1.2632	0.7774	0.628
dibenz[ <i>a,j</i> ]acridine .....	1.27	0.9717	0.7761	0.926
dibenz[ <i>c,h</i> ]acridine.....	1.29	0.9939	0.7774	0.867
dibenz[ <i>a,h</i> ]acridine.....	1.08	0.8733	0.7707	0.899
dibenz[ <i>a,c</i> ]acridine.....	1.59	1.4468	0.7769	0.916

NOTE.—Listed here are the calculated transition energies and electron affinities for the PANHs listed in Table 1. Experimental transition energies are listed for comparison, as well as a measure of the quality of the fit ( $\langle S^2 \rangle$ ).

intensities between 1500 and 500  $\text{cm}^{-1}$  (6.25–20  $\mu\text{m}$ ) to the total theoretical sum for the same region. This range was chosen to exclude the contributions of (1) the far-infrared bands ( $\nu < 500 \text{ cm}^{-1}$ ) that were not measured in the experiment, (2) the C-H stretching bands, whose intensities are substantially overestimated by the calculations (Bauschlicher & Langhoff 1997; Hudgins & Sandford 1998), and (3) the overtone/combination bands in the 2000–1650  $\text{cm}^{-1}$  (5–6.1  $\mu\text{m}$ ) region, whose intensities are not calculated in the theoretical results. This method takes advantage of the fact that, although there may be significant band-to-band variability in the accuracy of the calculated intensity, the total intensity is generally accurate to 10%–20%, excluding the C-H stretching region. Based on the total surface density of absorbers ( $N$ ) and the upper ionization limit (determined by the percent decrease in the integrated areas of the neutral mid-infrared bands

accompanying photolysis), one can calculate the number of ions present in each experiment and thus the integrated band strengths ( $A$  value, in  $\text{km mol}^{-1}$ ) for each band. These are presented in Table 1. Using these values, the spectra shown in Figures 1, 2, and 3 have been normalized to the same number of ions ( $1 \times 10^{15}$ ). Based on multiple experiments, ionization conversion efficiencies, and strong absolute band strengths, the uncertainty in band area determination and ultimate absorption strength is less than a factor of 2 for the entries in Table 1.

For presentation purposes only, the spectra have been baseline corrected and, in some instances, filtered, to lower noise, and the gas-phase  $\text{CO}_2$  purge contaminant features have been removed using the Win-IR Pro Software package. No further data reduction

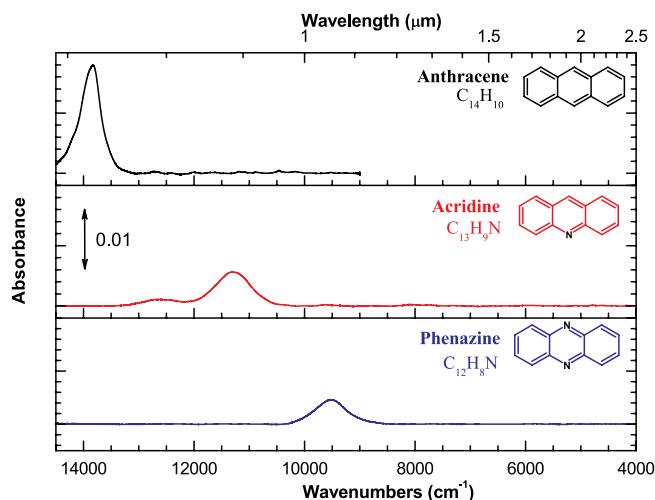


FIG. 1.—Argon matrix-isolated near-IR absorption spectra for the anthracene ( $\text{C}_{14}\text{H}_{10}$ ), acridine ( $\text{C}_{13}\text{H}_9\text{N}$ ), and phenazine ( $\text{C}_{12}\text{H}_8\text{N}_2$ ) cations. Spectra have been normalized to an equivalent number of ions ( $1 \times 10^{15}$ ).

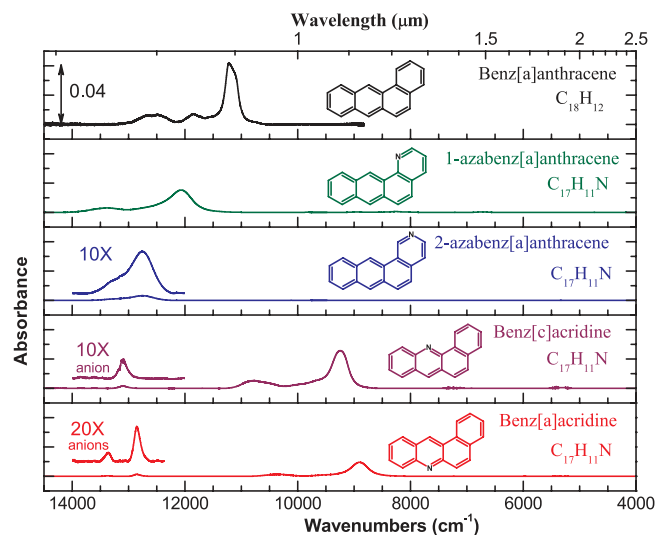


FIG. 2.—Argon matrix-isolated near-IR absorption spectra for the benzenanthracene, 1-azabenz[*a*]anthracene, 2-azabenz[*a*]anthracene, benz[*c*]acridine, and benz[*a*]acridine cations. All the PANHs are isomers with the formula  $\text{C}_{17}\text{H}_{11}\text{N}$ . Spectra have been normalized to an equivalent number of ions ( $1 \times 10^{15}$ ).

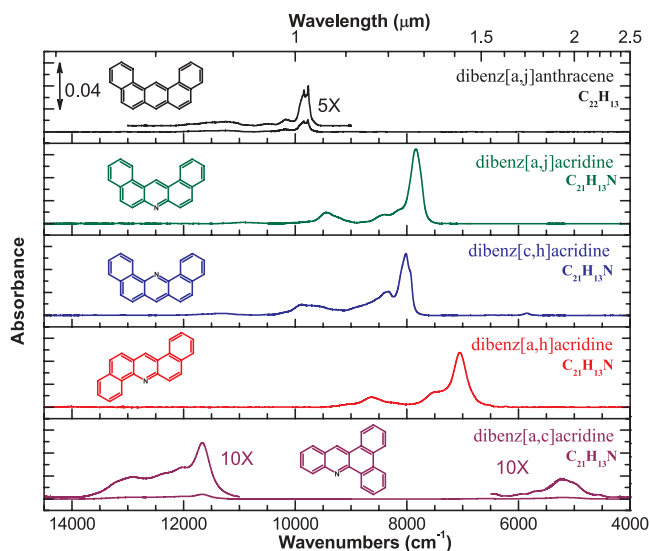


Fig. 3.—Argon matrix-isolated near-IR absorption spectra for the dibenzanthracene, dibenz[*a,j*]acridine, dibenz[*c,h*]acridine, dibenz[*a,h*]acridine, and dibenz[*a,c*]acridine cations. All the PANHs are isomers with the formula  $C_{21}H_{13}N$ . Spectra have been normalized to an equivalent number of ions ( $1 \times 10^{15}$ ).

was necessary. All numerical values used to derive the information in Table 1 were obtained from the original (unaltered) data.

### 2.2. Theoretical Methods

All calculations were performed on an Apple XServe Power PC G5 computer cluster, using the Q-Chem 3.0 program package (Shao et al. 2006). The ground-state geometry of all ions was optimized ignoring any apparent symmetry, and vibrational frequencies were also computed to characterize the stationary points, using unrestricted Kohn-Sham density functional theory with the B3LYP hybrid density exchange functional (Becke 1993; Hertwig & Koch 1997) with the 6-311  $G^*$  basis set for cations (Frisch et al. 1984). Subsequently, vertical excitations were calculated using time-dependent density functional theory (TDDFT; Dreuw & Head-Gordon 2005) at the unrestricted UB3LYP/6-311  $G^*$  level. Diffuse functions were not required owing to the very compact nature of excited states of cations. Oscillator strengths and attachment-detachment densities were also computed using full TDDFT. Values of the  $\langle S^2 \rangle$  operator for excited electronic states were calculated using the Tamm-Dancoff approximation (Hirata et al. 1999) to TDDFT. The level of spin contamination in the excited states (the deviation from ideal  $\langle S^2 \rangle$  values was less than 0.0445 in all cases, which is quite acceptable).

## 3. RESULTS

The near-infrared (NIR) spectra of the PANHs listed in the experimental section are shown in Figures 1, 2, and 3. The names, formulae, structures, deposition temperatures, individual and total integrated band strengths, and oscillator strengths are provided in Table 1. The PANHs are grouped and discussed as members of the corresponding, non-nitrogenated, parent PAH class. The NIR PANH spectra of the anthracene family are shown in Figure 1, the benzanthracene family in Figure 2, and the dibenzanthracene family in Figure 3.

### 3.1. Theoretical Results

As shown in Figure 4 and Table 2, the calculated vertical excitation energies generally agree well with the experimental data, predicting the absolute energies within roughly 0.25 eV.

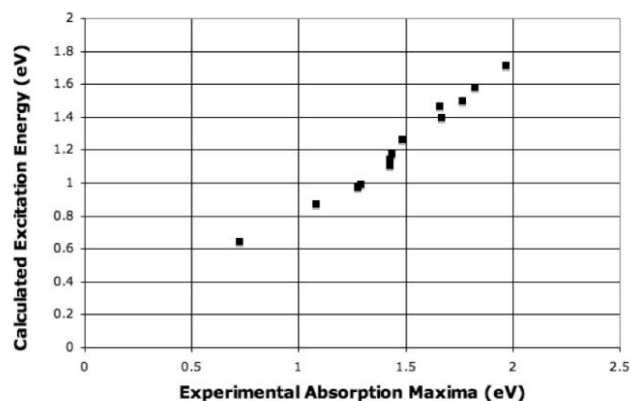


Fig. 4.—Correlation of calculated vertical excitation energies with experimental absorption energies for the molecules considered in this study.

This level of accuracy is roughly consistent with that seen for a very wide range of PAH cations (Hirata et al. 2003). The computational results provide a simple, intuitive model for understanding the absorption spectra in these related molecules.

In all but one special case, discussed below, the low-lying excited state with significant electronic absorption chiefly resulted from the promotion of an electron in the donor orbital into the lowest unoccupied molecular orbital (the acceptor orbital). The donor molecular orbital was frequently the second-highest occupied beta orbital, but not always. To understand the effect of nitrogen substitution in terms of the relative stabilization of the donor and acceptor orbitals, the electronic excitation can be viewed as a simple single electron transition from the donor to acceptor orbital. Due to its greater electronegativity than carbon, N substitution stabilizes an orbital that has substantial amplitude (electron density) on the atom where the nitrogen substitution occurs, but has relatively little effect on orbitals that have nodes (no electron density) or small amplitude on the C that is substituted by N. Thus either redshifts or blueshifts are possible for the electronic transition. Figure 5 demonstrates how this effect on the molecular orbitals of anthracene and acridine produces a redshift.

The nitrogen atom in most of the PANHs examined here were substituted in a position where the acceptor orbital possessed significant electron density, but the donor orbital did not, leading to an increase in stabilization, resulting in a redshift of the electronic transition. The calculations also correctly predict the relative amount of shift. However, a caveat must be imposed if the nitrogen substitution introduces a large change in the geometry of the molecule (if, for example, a hydrogen which was in steric contact with another is replaced with the lone pair of electrons on a nitrogen atom). Of course, such a substitution changes the shape of the orbitals in play, but it also mixes new excitations into the transition that compromise this simple model.

### 3.2. Near-Infrared Spectra of the Cations of the Nitrogenated Anthracenes: Acridine and Phenazine

Figure 1 shows the 14,500–4000  $cm^{-1}$  (0.690–2.5  $\mu m$ ) spectra of the anthracene, acridine, and phenazine cations. Peak positions and intensities are listed in Table 1. The NIR spectrum of the acridine cation shows one strong broad band (FWHM > 500  $cm^{-1}$ ) with a prominent shoulder to the blue. The spacing between the shoulder and main peak is roughly 1500  $cm^{-1}$ , a value similar to the vibronic spacing found for many PAH cations reported previously (Andrews et al. 1985; Mattioda et al. 2005b).



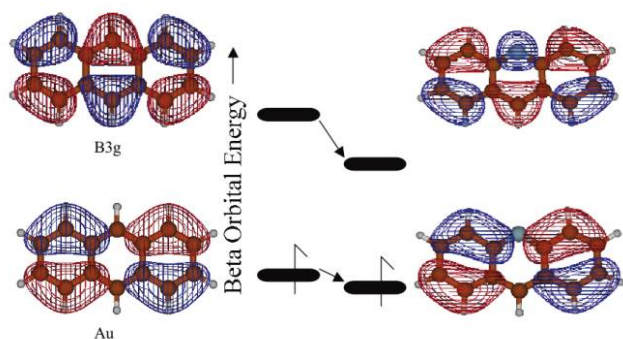


FIG. 5.—Molecular orbital diagram depicting the effect of nitrogen substitution on the electron donor (*top*) and acceptor (*bottom*) orbitals of the anthracene (*left*) and acridine (*right*) cations. The corresponding energy levels are given in the center. The size of the gap between these levels largely determines the transition energy. In the case shown here, the absorption in acridine is redshifted relative to anthracene

Assigning the strongest acridine cation NIR absorption band which peaks near  $11,300\text{ cm}^{-1}$  to the 0–0 transition, the  $1500\text{ cm}^{-1}$  spacing corresponds to the first member of the progression involving the C–C stretching vibration. However, the NIR spectrum of the dinitrogenated PANH phenazine does not exhibit such a progression.

The shapes of the donor and acceptor orbitals varied slightly with each geometry, but transitions of all these molecules can be understood as perturbations on the  $A_u \rightarrow B_{3g}$  transition of the anthracene cation (as shown in Fig. 5). The red and blue surfaces represent the electron density and the magnitude of the density present in the molecular orbitals, respectively. As discussed in § 3.1, the presence of a node falling at the position of nitrogen substitution in the donor orbital and the increase in electron density at that position in the acceptor orbital predict that nitrogen substitution should lower the energy of the acceptor orbital without changing the energy of the donor orbital (see Fig. 5). Based on this analysis, nitrogen substitution of one of the central carbon atoms in anthracene should decrease the energy gap between the electronic states, lowering the excitation energy and resulting in a redshift of the absorption band. This is borne out in the experimental results, with anthracene's main band situated around  $13,800\text{ cm}^{-1}$ , followed by acridine at  $11,306\text{ cm}^{-1}$ , and phenazine at  $9520\text{ cm}^{-1}$ .

### 3.3. Near-Infrared Spectra of the Cations of the Nitrogenated Benz[*a*]anthracenes: 1-azabenz[*a*]anthracene, 2-azabenz[*a*]anthracene, Benz[*c*]acridine, and Benz[*a*]acridine

Figure 2 shows the  $14,500\text{--}4000\text{ cm}^{-1}$  ( $0.690\text{--}2.5\ \mu\text{m}$ ) spectra of the benz[*a*]anthracene, 1-azabenz[*a*]anthracene, 2-azabenz[*a*]anthracene, benz[*c*]acridine, and benz[*a*]acridine cations. Peak positions and band intensities are listed in Table 1. As with the nitrogenated anthracenes, the NIR spectra of these nitrogenated benz[*a*]anthracene cations are dominated by a single broad band. The 1-azabenz[*a*]anthracene, benz[*c*]acridine, and benz[*a*]acridine cations show clear vibronic structure about  $1500\text{ cm}^{-1}$  to the blue of the strongest band. As in the case of acridine discussed above, this spacing corresponds to the first member of the progression involving the C–C stretching vibration. The spectrum of 2-azabenz[*a*]anthracene does not appear to show this structure, but rather has a prominent blue shoulder with a subpeak roughly  $500\text{--}600\text{ cm}^{-1}$  to the blue. The NIR spec-

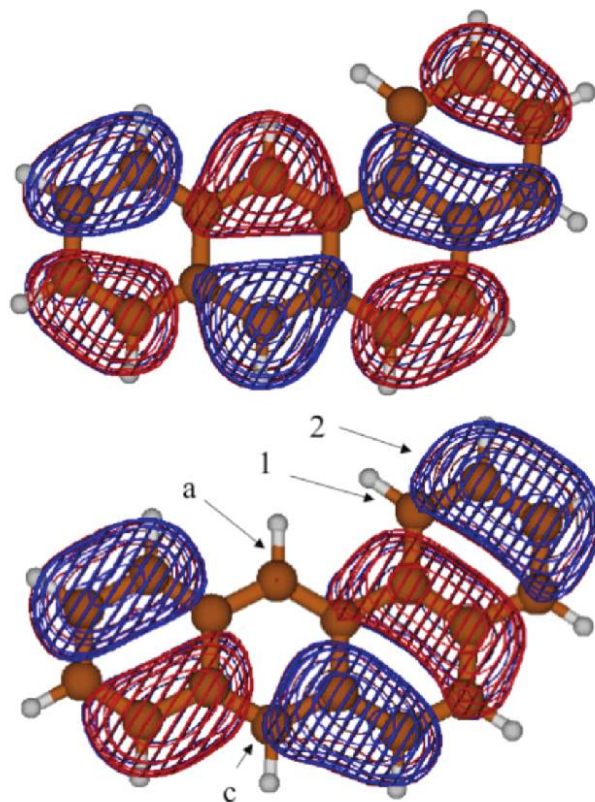


FIG. 6.—Donor (*bottom*) and acceptor (*top*) molecular orbitals of benz[*a*]anthracene. The positions of nitrogen substitution in 1-azabenz[*a*]anthracene, 2-azabenz[*a*]anthracene, benz[*a*]acridine and benz[*c*]acridine are indicated in the bottom (donor orbital) picture.

tra of photolyzed benz[*c*]acridine and benz[*a*]acridine are the only PANHs we have studied which exhibit anion features. For benz[*c*]acridine, a weak anion band peaks near  $13,100\text{ cm}^{-1}$ , and in the spectrum of benz[*a*]acridine here two weak anion bands are evident around  $12,900$  and  $13,400\text{ cm}^{-1}$ .

Although both benz[*a*]acridine and benz[*c*]acridine exhibit redshifts in peak positions similar to those observed for nitrogen insertion in the anthracene series, when nitrogen is inserted in the pendant ring in 1-azabenz[*a*]anthracene and 2-azabenz[*a*]anthracene, the main peak is blueshifted with respect to its position in benz[*a*]anthracene.

Applying the simple one electron orbital analysis developed above to the donor and acceptor orbitals of the parent PAH benz[*a*]anthracene (Fig. 6) explains both the redshift for benz[*a*]acridine and benz[*c*]acridine and blueshifts for 1-azabenz[*a*]anthracene and 2-azabenz[*a*]anthracene relative to the parent PAH. In the first two cases, the substitution of a nitrogen atom at a position of low electron density in the donor orbital but high electron density in the acceptor orbital narrows the energy gap, resulting in a redshift of the bands (see Figs. 2 and 6). The experimental results confirm this effect, with 1,2-benzanthracene exhibiting its main absorption feature at  $11,215\text{ cm}^{-1}$ , while benz[*a*]acridine and benz[*c*]acridine main absorptions occur at  $8910$  and  $9250\text{ cm}^{-1}$ , respectively. However, the situation is different for 1-azabenz[*a*]anthracene and 2-azabenz[*a*]anthracene, where the position of nitrogen substitution has a greater electron density in the donor orbital relative to the acceptor orbital in the parent PAH (see Fig. 6). Thus, the energy of the donor orbital decreases more than the energy of the acceptor orbital, and so the gap between the two, which is

tied to the excitation energy, increases on nitrogen substitution, resulting in a blueshift. This shift is evident in Figure 2, where the absorption feature for 1-azabenz[*a*]anthracene and 2-azabenz[*a*]anthracene fall at 12,076 and 12,762  $\text{cm}^{-1}$ .

As noted previously, the presence of an anion was noted in the spectra of benz[*a*]acridine and benz[*c*]acridine. The electron affinities of the neutral species considered in this study were also estimated by calculating the difference between the electronic energy of the neutral and the anion at their optimized geometries (both with the 6-311+G\* basis set). The calculated electron affinities reproduce trends one would expect, increasing with nitrogen substitution and the size of the conjugated system (Table 2). The two species with anion bands had high electron affinities compared to their four-ringed non-nitrogenated peers, as expected, but are not exceptional with respect to the other nitrogenated PANHs considered here.

### 3.4. Near-Infrared Spectra of the Cations of the Nitrogenated Dibenzanthracenes: Dibenz[*a,j*]acridine, Dibenz[*c,h*]acridine, Dibenz[*a,h*]acridine, and Dibenz[*a,c*]acridine

Figure 3 shows the 14,500–4000  $\text{cm}^{-1}$  (0.69–2.5  $\mu\text{m}$ ) cation spectra of dibenz[*a,j*]anthracene compared to its nitrogen-substituted dibenz[*a,j*]acridine and dibenz[*c,h*]acridine analogs, as well as the spectra of dibenz[*a,h*]acridine and dibenz[*a,c*]acridine cations. The peak positions and band intensities for all molecules are listed in Table 1. As shown in Figure 7, the donor orbitals for the parent PAH dibenz[*a,j*]anthracene exhibit very little, if any, electron density on the central carbon atoms. Thus, based on the previous discussions, one would expect nitrogen substitution in either the [*a,j*] or [*c,h*] positions to produce a redshift in the band positions. Furthermore, the small amount of electron density at the [*c,h*] position versus a node at the [*a,j*] position should result in slightly less of a redshift for dibenz[*c,h*]acridine. This matches quite nicely with the experimental results. Dibenz[*a,j*]anthracene's main absorption feature is at 9773  $\text{cm}^{-1}$ , which becomes redshifted to 8016  $\text{cm}^{-1}$  on insertion of a nitrogen atom at the [*c,h*] position, forming dibenz[*c,h*]acridine. Placement of the nitrogen atom in the [*a,j*] position results in the band center being shifted to 7837  $\text{cm}^{-1}$  (see Table 1 and Fig. 3). Dibenz[*a,h*]acridine, which is unrelated to dibenz[*a,j*]anthracene, exhibits its main absorption feature at 7044  $\text{cm}^{-1}$ .

The vibronic structure of the prominent bands in the NIR spectra of all these PANH cations is striking and somewhat unusual for the PAHs and PANHs studied to date. In all four cases, the most prominent transition is blended with a band centered approximately 400  $\text{cm}^{-1}$  to the blue and has a separate weaker companion with a spacing of about 1500  $\text{cm}^{-1}$ . Mattioda et al. (2003) reported that the insertion of nitrogen into a PAH tends to enhance the strength of the C-C and C-H in-plane vibrations, similar to the effect observed on ionization. Likewise, as discussed in Mattioda et al. (2003, 2008, in preparation), the presence of nitrogen in a position para (opposite) to a C-H group tends to greatly enhance a C-C in-plane vibration around 1400  $\text{cm}^{-1}$ . As previously discussed, the 1500  $\text{cm}^{-1}$  vibronic spacing is most likely due to the enhanced C-C and C-H in-plane modes. Unfortunately, the source of the 400  $\text{cm}^{-1}$  spacing is ambiguous, partly due to the limited spectroscopic data below 500  $\text{cm}^{-1}$ .

Interestingly, the NIR spectrum of dibenz[*a,c*]acridine shows evidence for two different electronic transitions with 0–0 positions near 5200 and 11,700  $\text{cm}^{-1}$ . The computed vertical excitation spectrum explains both absorptions and their relative energies. The experimental peak near 5200  $\text{cm}^{-1}$  resembles the anthracene-type transition in terms of transition dipole, orbital contributions, and attachment-detachment densities (Head-Gordon et al. 1995;

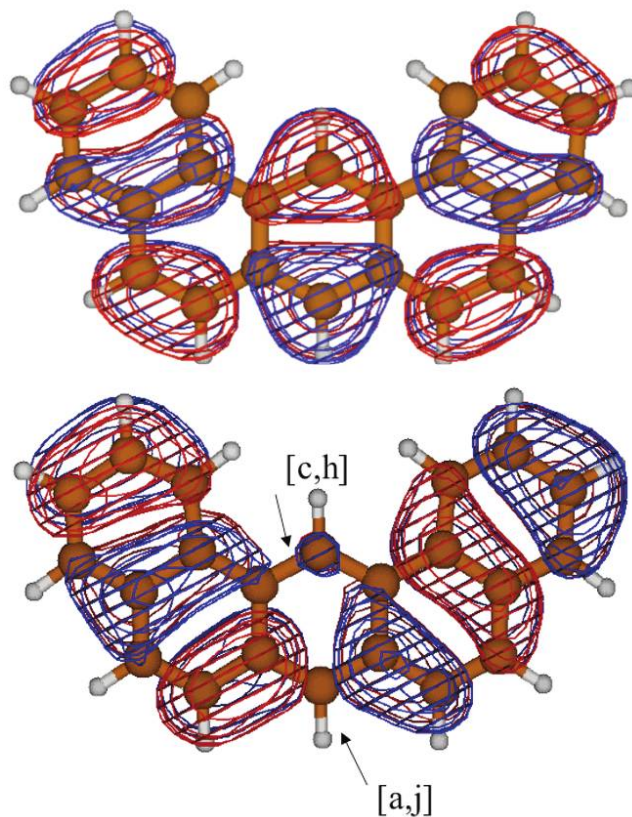


FIG. 7.—Donor (bottom) and acceptor (top) molecular orbital for dibenz[*a,j*]anthracene. The nitrogen atom positions for dibenz[*c,h*]acridine and dibenz[*a,j*]acridine are indicated in the figure.

see below). Relative to its parent PAH, which is not included in the experimental data set, the simple model predicts that it should be redshifted by nitrogen substitution in dibenz[*a,c*]acridine. TDDFT calculations on that compound support this conclusion. The higher energy transition at 11,700  $\text{cm}^{-1}$  results from a state unlike those seen in the other molecules. Unlike the single donor molecular orbitals observed for the other PANHs and PAHs discussed, the TDDFT excitation for dibenz[*a,c*]acridine contains significant contributions from four donor orbitals, one of which is shown in Figure 8. In cases such as this, it is useful to examine the attachment-detachment electron densities, which schematically picture the movement of electron density in a before (ground state)–and–after (excited state) fashion, instead of the donor/acceptor orbitals. As shown in Figure 8, the nitrogen atom is substituted in a position of low electron density in the electron detachment density (i.e., in lieu of the donor orbital), but high electron density in the electron attachment density (i.e., in lieu of the acceptor orbital). Thus, according to our results, one should expect to observe a redshift from the band position in the non-nitrogenated parent PAH (dibenz[*a,c*]anthracene). Although dibenz[*a,c*]anthracene was not measured experimentally, the calculations predict this transition to occur at a higher frequency than that observed in the nitrogenated PAH. The plots demonstrate that the high-energy transition is another sort of  $\pi \rightarrow \pi^*$  excitation.

### 3.5. Near-Infrared Band Intensities

Integrated absorbance values ( $\text{km mol}^{-1}$ ) for the bands in the spectra shown in Figures 1, 2, and 3 are listed in Table 1. As in Mattioda et al. (2005b), the band strengths of these electronic



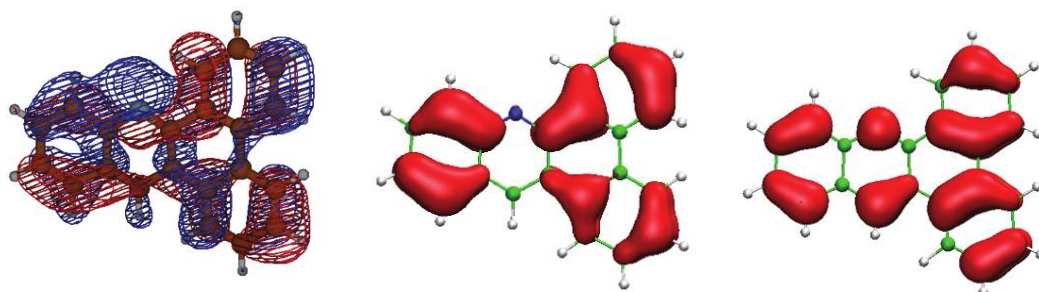


FIG. 8.—Electron distributions for the dibenz[*a,c*]acridine 11,700  $\text{cm}^{-1}$  excitation. The first image is one of the four donor beta orbitals. The electron detachment density, to be used in lieu of the donor orbital, is the second image, while the third image represents the electron attachment density, to be used in lieu of the acceptor orbital image.

transitions are presented in oscillator strength,  $f$ , and in units of  $\text{km mol}^{-1}$  to facilitate comparisons with mid-IR band strengths, which are normally presented in  $\text{km mol}^{-1}$ . See Mattioda et al. (2005b) for a detailed description of the procedure used to determine these absorption strengths. The oscillator strength was determined by multiplying the total integrated absorbance by  $1.87 \times 10^{-7}$  mole  $\text{km}^{-1}$  (Kjaergaard et al. 2000).

For the transitions of the PANHs considered here, the oscillator strengths range from  $1.3 \times 10^{-3}$  to  $4.2 \times 10^{-2}$ , a range somewhat similar to that reported for PAHs of approximately the same size in Mattioda et al. (2005b).

A comparison can be made between the nitrogenated PAH and its parent molecule. For the anthracene series it appears that the insertion of a single nitrogen has little impact on the total oscillator strength. While anthracene exhibits an oscillator strength of  $9.0 \times 10^{-3}$ , acridine has a value of  $6.0 \times 10^{-3}$ . The oscillator strength is lowered to  $3.1 \times 10^{-3}$  for phenazine, which contains two nitrogen atoms. This is similar to the trend displayed in the calculated values, which shows phenazine exhibiting a slightly lower oscillator strength than either anthracene or acridine.

TDDFT is often a useful tool for predicting trends in oscillator strengths (Halasinski et al. 2003), although they are more prone to error than the transition frequencies themselves (Appel et al. 2003). The B3LYP hybrid functional has been used for this purpose in the past (Zdetsis et al. 2001); however, in this instance the agreement with experiment is somewhat unsatisfactory, although similar to that observed in Mattioda et al. (2005b). The neglect of Franck-Condon factors in the calculation of the vertical excitation spectrum may be partly responsible for the difference between calculated and experimental oscillator strengths. Likewise, the comparison of gas-phase values (theoretical calculations) to matrix-isolated experimental values may be responsible for some of the differences. Still, some basic things can be inferred from the transition moment. The molecules with a  $C_2$  symmetry axis perpendicular to the plane of the molecule have a transition moment directed with the long axis. Thus, the substitution of carbon for nitrogen in the center of the molecule should not have a large effect on the transition dipole, and by association the oscillator strength. This is in line with the experimental observations for the three-ringed systems, and certainly in agreement with the calculations.

For the benz[*a*]anthracene series, it is difficult to tell what influence nitrogen insertion has on the oscillator strength of the NIR transition. The total oscillator strengths for 1-azabenz[*a*]anthracene and benz[*c*]acridine are similar to that observed in the parent PAH, approximately  $2 \times 10^{-2}$ . However, the total oscillator strengths of 2-azabenz[*a*]anthracene and benz[*a*]acridine are nearly an order of magnitude lower (see

Table 1). Theoretical calculations display little variation in oscillator strength between molecules in this series.

The total oscillator strength of dibenz[*a,j*]acridine, dibenz[*c,h*]acridine, and dibenz[*a,h*]acridine are significantly larger than dibenz[*a,j*]anthracene, while the transitions noted in dibenz[*a,c*]acridine are on the same order. This is in contrast to the theoretical values, which display little variation between dibenz[*a,j*]anthracene, dibenz[*a,j*]acridine, dibenz[*c,h*]acridine, and dibenz[*a,h*]acridine, but a significantly lower value for the oscillator strength of dibenz[*a,c*]acridine (see Table 1).

In spite of its fundamental astrophysical importance, determining reliable PAH ion oscillator strengths for electronic transitions experimentally has proven particularly challenging (Hudgins & Allamandola 1995b; Salama & Allamandola 1991). Due to the inherent difficulty in maintaining a stable, isolated PAH ion population, the vast majority of spectroscopic studies have been carried out in inert gas matrices. Comparisons between gas-phase and matrix-isolation spectroscopic studies with quantum calculations have shown that matrix perturbations are minor when studying PAH ion *vibrational* transitions, which give rise to the well-known interstellar infrared emission bands (e.g., Hudgins & Allamandola 2004; Mattioda et al. 2003), and matrix-isolation studies can be directly applied to the interstellar IR emission bands. This is *not* generally so for electronic transitions, which give rise to bands spanning the UV to the NIR spectral range. As discussed in Mattioda et al. (2005a, 2005b, 2005c), the PAH NIR band shifts and FWHH variations between argon and neon matrices and gas-phase studies show that the matrix environment can severely perturb intrinsic *electronic* band positions and band shapes. Electronic transition band strengths are perturbed as well. The matrix influence on band strengths for electronic transitions are not only matrix dependent, but are also influenced by other species present in the matrix (Hudgins & Allamandola 1995a). To make matters worse, it also appears to depend on the method of determination. For example, Salama et al. (1994) studied the electronic transition [ $D_2 \leftarrow D_0$ ] of the neon matrix isolated phenanthrene cation, corresponding to the same transition reported in Mattioda et al. (2005a, 2005b, 2005c), for phenanthrene in an argon matrix. Salama et al. (1994) calculated the number of phenanthrene ions produced from the reduction in the absorbance of the neutral phenanthrene *electronic* bands in the UV. This is in contrast to the method employed by Mattioda et al. (2005a, 2005b, 2005c), the same method employed here, in which the number of phenanthrene ions produced is determined by the reduction in the absorbance of the neutral phenanthrene *vibrational* bands in the mid-IR. The discrepancy is unacceptably large. Salama et al. report an  $f$  value of  $6 \times 10^{-5}$  for this phenanthrene cation transition in a neon matrix, while Mattioda

et al. report  $f = 3.5 \times 10^{-3}$  from the argon matrix data. These values are to be compared with theoretical values, which range from 0.096 to 0.16. It is also interesting to note that Bréchniga & Pino (1999) measured this transition for the phenanthrene cation in the gas phase. They determined an oscillator strength of 0.150, which is in good agreement with the theoretical predictions, but at odds with the matrix work. Another example of a significant discrepancy originating in the method used to determine the number of ions produced is provided by the anthracene cation. Our value of 0.009 for the oscillator strength of the  $13,835 \text{ cm}^{-1}$  band of the anthracene cation in an argon matrix is an order of magnitude lower than the value of 0.08 measured for the anthracene cation in argon matrix by Szczepanski et al. (1993). In this case, the value determined by Szczepanski et al. (1993) is in better agreement with the theoretical prediction of about 0.1.

To the best of our knowledge, the pyrene and coronene cations are the only other PAH cation for which theoretical and experimental NIR experimental oscillator strengths have been reported. In contrast to the theoretical value of 0.015 for the  $[\pi_0^* \leftarrow \pi_{-2}]$  transition in pyrene (Hirata et al. 2003), Vala et al. (1994) report  $f \sim 0.005$ , compared to value of  $f \sim 0.0015$  (Mattioda et al. 2005a, 2005b, 2005c). For coronene, however, the agreement is better. Hirata et al. (2003) predicted a value of 0.006 for the  $[\pi_0^* \leftarrow \pi_{-3}]$  transition, while Ehrenfreund et al. (1995) have measured the NIR spectrum for the coronene cation isolated in an argon matrix and determined  $f \sim 0.005$ , a value that compares favorably with the  $f \sim 0.006$  reported by Mattioda et al. (2005a, 2005b, 2005c). In summary, there is a large variation in reported PAH ion oscillator strengths, regardless of means of determination. In those cases for which argon matrix data is available, differences of a factor of 2–10 are encountered. Inspection of Table 1 in Mattioda et al. (2005a, 2005b, 2005c) shows that, when theoretical data are available, most of the experimental values are 1.3–10 times smaller. For the PANH NIR spectra reported here, the experimental values vary between 5 and 15 times smaller than the theoretical results. The origin of this serious discrepancy between the few available gas-phase oscillator strength and matrix values is unknown, but may be related to the evaluation of the density of cations in the matrix.

#### 4. ASTROPHYSICAL CONSIDERATIONS

The spectra shown in Figures 1, 2, and 3 and corresponding absolute absorption strengths listed in Table 1 illustrate that PANH cations have NIR transitions that should be taken into account when evaluating the effects of PAHs and PANHs on the interstellar radiation field. Following Mattioda et al. (2005b), we consider two applications that impact observations, the role of NIR photons in pumping the mid-IR PAH/PANH emission bands, and the possibility that PANHs can impose broadband structure on the interstellar extinction curve in addition to contributing to the discrete diffuse interstellar bands (DIBs).

However, before proceeding further it is necessary to discuss two issues concerning the previous PAH NIR investigation (Mattioda et al. 2005b, 2005c), which came to light during the course of the PANH NIR investigation. Although neither issue impacts the relevant findings of the earlier investigation, these items should be addressed. The first issue relates to equation (5) of Mattioda et al. (2005c). A programming error resulted in incorrect parameters being reported for  $S_1$ ,  $S_2$ , and  $S_3$ , of equation (5) in Mattioda et al. (2005c), here corrected as our equation (1):

$$\frac{\sigma_{\text{abs}}^{\text{PAH}}(\lambda)}{N_{\text{C}}} = 3.5 \times 10^{-19-1.45\lambda/\mu\text{m}} \frac{\text{cm}^2}{\text{C atom}} + S_1 + S_2 - S_3, \quad (1)$$

TABLE 3  
CORRECTED PARAMETERS FOR MATTIODA ET AL. 2005c EQUATION (5),  
OUR EQUATION (1)

Drude	$\lambda_j$ ( $\mu\text{m}$ )	$\gamma_j$	$A_{\text{int},j}$ ( $\text{cm}^2 \mu\text{m}^{-1} \text{C}^{-1}$ )
$S_1$ .....	1.05	0.055	$2.0 \times 10^{-20}$
$S_2$ .....	1.26	0.11	$7.8 \times 10^{-21}$
$S_3$ .....	1.905	0.09	$1.465 \times 10^{-22}$
Gaussian	$\lambda_0$ ( $\mu\text{m}$ )	$w_j$	$A$ ( $\text{cm}^2 \mu\text{m}^{-1} \text{C}^{-1}$ )
$G$ .....	1.185	0.2985	$1.40 \times 10^{-20}$

where  $S_j$  represents Drude profiles given by

$$S_j(\lambda) = \frac{2}{\pi} \frac{\gamma_j \lambda_j A_{\text{int},j}}{(\lambda/\lambda_j - \lambda_j/\lambda)^2 + \gamma_j^2}. \quad (2)$$

For this equation,  $\gamma_j$  is a broadening parameter,  $\lambda_j$  is the central wavelength of a feature in  $\mu\text{m}$ , and  $A_{\text{int},j}$  is the integrated absorption strength expressed in cm per C atom ( $\sigma_{\text{int},j}$  in Draine & Li 2001). The correct parameters are listed in Table 3.

The second issue concerns the impact of this adjustment on the NIR PAH portion of the graphs presented in Figure 8 of Mattioda et al. (2005b) and Figure 1 in Mattioda et al. (2005c), which represent the composite spectrum of 27 equally weighted PAH spectra. We have improved our spectral averaging routine. A comparison between the new PAH composite spectrum is shown with the originally published data in Figure 9. As one can see, the differences between the old and new composites are minor, with the most obvious differences being a narrowing of the  $1 \mu\text{m}$  feature and elimination of the small bands at 1.66 and  $1.75 \mu\text{m}$ . These differences were caused by a transcription error, which resulted in the spectrum of one PAH molecule being given more weight in the overall average. The overemphasis of this molecule was responsible for the 1.66 and  $1.75 \mu\text{m}$  features as well as the broadening of the  $1 \mu\text{m}$  band. Finally, we should also mention the dip that occurs around  $1.9 \mu\text{m}$  in the original composite spectrum. Figure 9 shows that  $\text{CO}_2$  overtone bands from the purge gas produce an artifact at this position.

Although the changes result in a slightly altered composite spectrum, they do not change the overall conclusion that open-shell PAHs exhibit NIR absorptions which could pump mid-IR emission in areas of low UV flux as well as add detectable structure to the interstellar extinction curve.

##### 4.1. Pumping the Mid-IR PAH/PANH Emission Features with NIR Photons

An important, long-standing issue concerning the model that IR fluorescence from highly vibrationally excited PAHs is responsible for the interstellar mid-IR emission features involves the excitation mechanism. To properly test this aspect of the PAH excitation/emission model and put it on as quantitative a footing as possible requires a deeper understanding of the complete UV-visual-NIR spectroscopic properties of PAHs and related species (ions, hetero-atom substituted, etc.) than is currently available. This NIR spectroscopic study of PANH cations contributes some of this information.

The experimental NIR spectra for a wide variety of PAH ions has permitted a revision in the PAH ion optical radiation absorption model (Mattioda et al. 2005a). A semiempirical model,

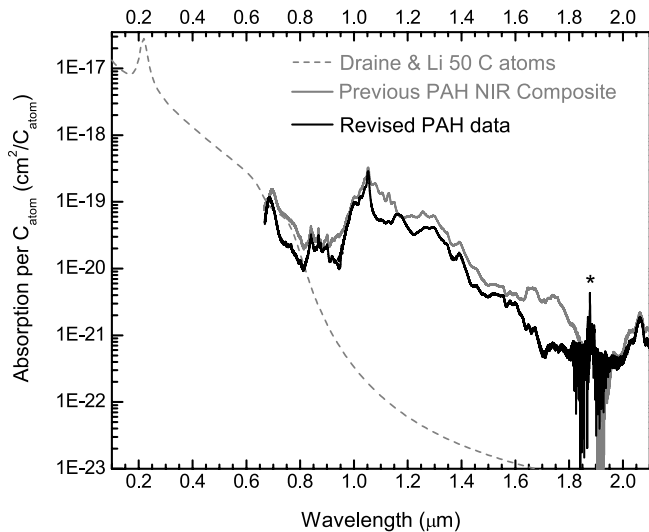


FIG. 9.—Comparison of initial PAH composite spectrum with the revised PAH composite and the Draine & Li curve. Note the purge CO<sub>2</sub> overtones overlapping the 1.9 μm feature.

which takes into account the significant NIR absorption features of PAH ions, has been proposed (Mattiola et al. 2005b). After combining these PAH cation NIR spectroscopic properties with the Draine & Li (2001) PAH UV-visual optical model, a comparison was made between the energy absorbed by PAH ions in the NIR and that of the UV-visual region for a wide array of stellar classes. This comparison reveals that for lower temperature stars, NIR energy absorption becomes increasingly important, matching the energy absorbed from the UV-visual for late K and M stars. Thus, even in areas of low UV flux, absorption in the NIR could stimulate mid-IR emission from PAH ions. In a recent publication, Draine & Li (2007) have incorporated these optical radiative properties as part of a very thorough and complete model of interstellar extinction and dust radiative properties that is used to interpret *Spitzer* observations of a very wide variety of objects.

Here we revisit the semiempirical PAH optical property model presented by Mattiola et al. (2005b), and incorporate the NIR spectroscopic properties of PANH ions presented here.

The upper portion of Figure 10 displays the revised PAH NIR composite spectrum, as well as the composite spectrum of the 10 PANH ions that were part of this investigation. Although it extends slightly more into the red, the composite peak of the PANH spectrum nicely matches that of the PAH spectrum. The main difference, on averaging the PANH and PAH data (see lower portion of Fig. 10), is the slight extension of the composite “bump” into the red (by <0.1 μm).

Figure 11 displays the composite PAH PANH NIR cation spectrum as well as the fit to this new data. This fit is given by

$$\frac{\sigma_{\text{abs}}^{\text{PAH}}(\lambda)}{N_{\text{C}}} = 1.4 \times 10^{-19.2-1.34\lambda/\mu\text{m}} \frac{\text{cm}^2}{\text{C atom}} + \frac{A}{w\sqrt{\pi/2}} e^{-2(\lambda-\lambda_0)^2/w^2}, \quad (3)$$

where the wavelengths are in μm, λ<sub>0</sub> is the center of the peak in μm, w is twice the standard deviation of the Gaussian distribution (2 × σ) or approximately 0.849, the width of the peak at half height in μm, and A is the area under the peak. The actual values for the Gaussian portion of the curve are provided in Table 3. These

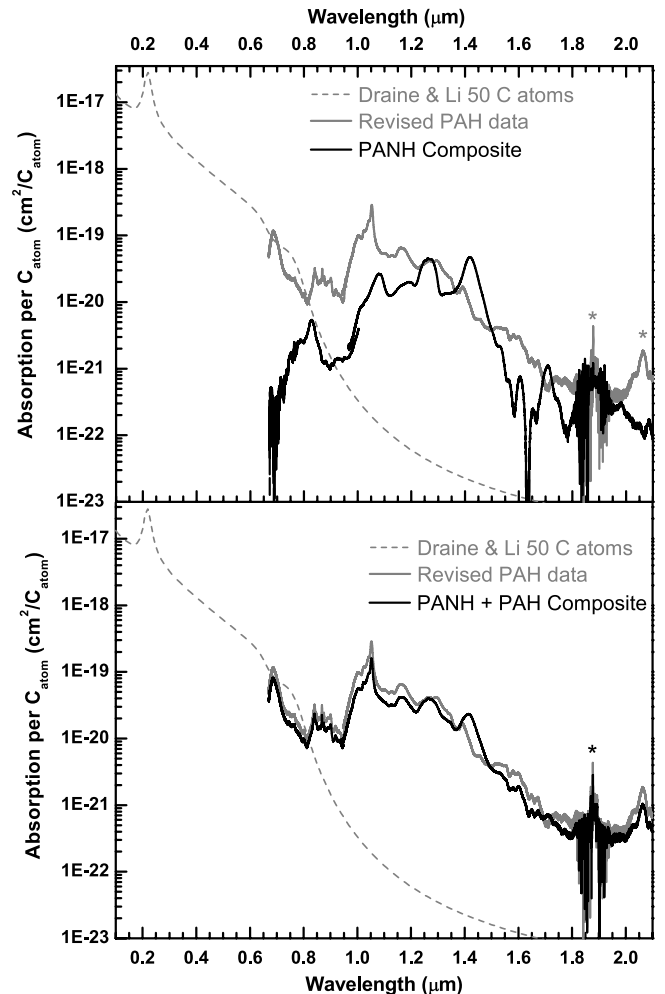


FIG. 10.—*Top*: Comparison of the PAH composite NIR spectrum comprising 27 PAH ions vs. the PANH composite spectrum composed of 10 PANH ions with the original Draine & Li (2001) astronomical PAH spectrum. *Bottom*: Comparison of the PAH composite and the total PANH/PAH composite spectrum with the initial Draine & Li (2001) astronomical PAH spectrum.

parameters are valid for the region between 0.82 and 1.82 μm, after this point the baseline becomes a nearly constant value of  $3.35 \times 10^{-22} \text{ cm}^2/\text{C atom}$ .

Equation (3) and Figure 11 reveal that the overall character of the composite PAH PANH NIR cation spectrum can be fit reasonably well with a single Gaussian curve centered around 1.185 μm. Of course, such a fit neglects the substructure apparent in Figure 11. However each component of the apparent substructure is the result of one or two fairly intense PAH/PANH cation bands. The intent of this fit is to provide a model for the absorption of a mixture of open-shell PAH and PANH molecules in the interstellar environment. The new composite PAH-PANH spectrum is the result of 38 equally weighted PAH and PANH cation spectra. In the interstellar environment one would expect a more complex mixture of PAH species, exhibiting different weights for each of the species. As Figure 11 demonstrates, such a mixture should result in a feature visible around 1.2 μm, not accounting for the matrix shift. Such a matrix shift, as pointed out in Mattiola et al. (2005b), may produce a similar band, but redshifted by  $\sim 100 \text{ cm}^{-1}$ , as was the case for the phenanthrene cation. Of course, sharper features may be evident on the extinction curve if a few astronomical PAHs or PANHs are particularly strong. This is discussed in further detail below.

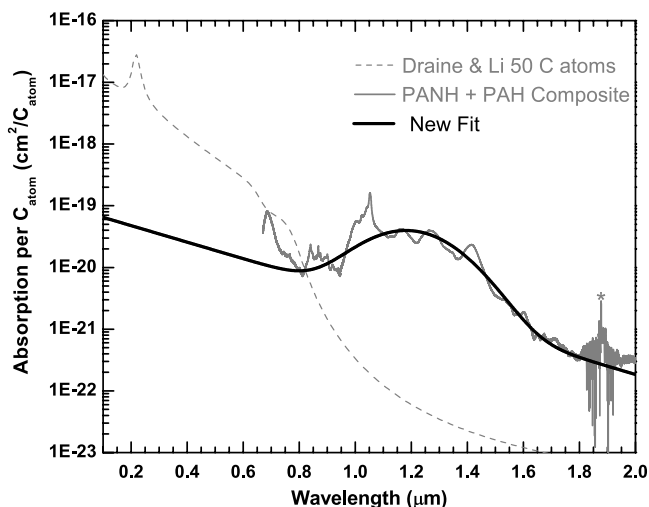


FIG. 11.—Fit to the PANH+PAH NIR composite spectrum using eq. (3) and the parameters listed in Table 3.

#### 4.2. Interstellar PAHs and the Extinction Curve

There is overwhelming evidence that ionized PAHs are widespread throughout the diffuse ISM (Mattila et al. 1996; Onaka et al. 1996). As shown in the previous section, NIR transitions in these and PAH-related species, such as PANHs, could impose detectable structure on the extinction curve. Here we extend our earlier estimation of the extent to which this is possible (Mattioda et al. 2005a) to include PANHs. As in the PAH study, the cases considered are somewhat contrived, as there are likely many hundreds if not hundreds of thousands of different PAH/PANH molecular structures that could contribute spectroscopic structure to the extinction curve. Knowing neither the different structures nor their corresponding spectra, we approximate the situation as follows. Using the standard relationship  $N_{\text{H}}/E(B-V) = 5.8 \times 10^{21} \text{ atoms cm}^{-2} \text{ mag}^{-1}$  (Bohlin et al. 1978), where  $N_{\text{H}}$  is the number of hydrogen atoms per  $\text{cm}^2$  along the line of sight and  $E(B-V)$  is the reddening expressed in magnitudes. Taking  $3 \times 10^{-4}$  for the cosmic C/H ratio, the number of carbon atoms per  $\text{cm}^2$  per  $E(B-V)$  becomes  $N_{\text{C}}/E(B-V) = 1.7 \times 10^{18}$ . Assuming 10% of the available cosmic carbon is in the form of free PAHs (e.g., Allamandola et al. 1989; Puget & Leger 1989), the number of C atoms tied up in free PAHs per  $\text{cm}^2$  per  $E(B-V)$  is then  $N_{\text{C-PAH}}/E(B-V) = 1.7 \times 10^{17}$ . This is, however, a very conservative lower limit for the total amount of cosmic carbon tied up in PAH structures, since the 10% value for the amount of available carbon in PAHs holds for those contributing to the mid-IR emission features. Larger PAHs, PAH clusters, and amorphous carbon particles rich in PAH structures that do not contribute to the mid-IR features must also be present, and many of these will also have NIR transitions. However, for the sake of this analysis we assume an average of 50 C atoms per PAH. In this case,  $N_{\text{PAH}} = 3.4 \times 10^{15} E(B-V)$  molecules  $\text{cm}^{-2}$ .

Assuming a situation in which 10% of the PAHs in the total PAH ion population all absorb at nearly the same wavelength, the optical depth ( $\tau = \ln I_0/I$ ) of a band in the NIR portion of the extinction curve produced by these PAHs is estimated as follows. The spectra and integrated absorbance values presented in § 3 show that PAH cations containing between 40 and 50 C atoms often possess a discrete absorption band near  $9000 \text{ cm}^{-1}$  ( $1.1 \mu\text{m}$ ) with a FWHM  $\sim 400 \text{ cm}^{-1}$  ( $\sim 0.04 \mu\text{m}$ ), having integrated absorbance values ( $A$ ) between roughly  $1.6 \times 10^5$  and  $6.9 \times 10^5 \text{ km mol}^{-1}$  ( $2.56 \times 10^{-14}$  and  $1.1 \times 10^{-13} \text{ cm molecule}^{-1}$ ). Since  $N_{\text{PAH}}A \approx$

$(\tau)dv$ , the optical depth becomes  $N_{\text{PAH}}A/dv$ . Taking  $A \approx 5 \times 10^{-14} \text{ cm molecule}^{-1}$ ,  $dv = 400 \text{ cm}^{-1}$ , and  $N_{\text{PAH}} = 3.4 \times 10^{14} E(B-V)$  molecules  $\text{cm}^{-2}$  (for 10% of the PAH ion population) yields a  $\tau/\text{mag} = 0.04$  for an absorption band produced by these interstellar PAH molecules.

Thus, the data presented here suggest that there should be weak, but detectable, broadband structure originating in ionized PAHs and PANHs superposed on the NIR portion of the interstellar extinction curve.

#### CONCLUSIONS

Since very little near-infrared (NIR) spectroscopic data were available for ionized PANHs, a systematic study of the NIR spectroscopic properties of argon matrix-isolated PANH ions has been undertaken. Here we report the NIR spectra and absolute band strengths of 10 nitrogen-containing polycyclic aromatic hydrocarbon (PAH) cations. These include the nitrogenated anthracenes, acridine ( $\text{C}_{13}\text{H}_9\text{N}$ ) and phenazine ( $\text{C}_{12}\text{H}_8\text{N}_2$ ); the four isomeric nitrogenated benzanthracenes, 1-azabenz[*a*]anthracene, 2-azabenz[*a*]anthracene, benz[*c*]acridine, and benz[*a*]acridine, all with formula  $\text{C}_{17}\text{H}_{11}\text{N}$ ; and the four isomeric nitrogenated dibenzanthracenes, dibenz[*a,j*]acridine, dibenz[*c,h*]acridine, dibenz[*a,h*]acridine, and dibenz[*a,c*]acridine, all with formula  $\text{C}_{21}\text{H}_{13}\text{N}$ . As with ionized PAHs, all the ionized PANHs we have studied have strong, broad absorption bands in the NIR, arising from electronic transitions. Oscillator strengths and integrated absorbance values have been determined for these NIR transitions.

All of these NIR spectra are dominated by a strong, broad (FWHM  $\sim 500 \text{ cm}^{-1}$ ) band corresponding to the 0–0 transition, and most show clear, weaker, vibronic substructure to the blue. The vibronic bands correspond to progressions involving the CH out-of-plane bends and C-C stretching vibrations. Some PANHs also show vibronic bands with unusual spacing of about  $400 \text{ cm}^{-1}$ , consistent with the difference between an unusually strong C-N-C and C-H in-plane vibration (around  $1400 \text{ cm}^{-1}$ ) and that of the C-H out-of-plane modes. None of the argon matrix-isolated, PANH cation, NIR spectra show sharp features as is the case for some PAHs (Mattioda et al. 2005a).

TDDFT is an appropriate model for the large cations discussed in this study. The theoretical modeling shows that in this series of anthracene derivatives, the band shift direction can be predicted by the relative magnitudes of the donor and acceptor molecular orbitals present at the position of the nitrogen substitution in the parent PAH. Most of the PANHs examined here were substituted with nitrogen at a position where the acceptor molecular orbital possessed significant electron density, but the donor orbital did not, leading to redshifts.

Two astrophysical applications have also been considered. The first has to do with the radiation fields that pump the interstellar IR emission bands. The data presented here show that open-shell PANH ions have significant absorption features in the near-infrared, similar to the situation for PAH ions. A quantitative treatment of PAH and PANH optical properties spanning the UV-visual-NIR spectral is presented. The second astrophysical application has to do with interstellar extinction. Since the spectra of ionized PANHs show strong NIR transitions, and PANHs are very likely to be present and abundant in the interstellar medium, they could add detectable structure to the extinction curve. A quantitative estimate is made of this potential extinction. The band strengths reported here suggest that ionized interstellar PANHs should add weak, broadband structure to the NIR portion of the interstellar extinction curve between 1 and  $1.6 \mu\text{m}$ .

As with PAHs, it is also important to keep in mind that some structures of neutral PANHs can also have open-shell, radical

electronic configurations, as do the ions studied here (e.g., Hudgins et al. 2001, 2005; Szczepanski et al. 2002), and these will also possess longer wavelength electronic transitions, albeit likely having lower cross sections than ionized open-shell species. Thus, even in regions dominated by non-ionizing radiation, it may be possible to detect the emission from neutral, open-shell PANH species.

The experimental portion of the research presented here was supported through NASA's Long Term Space Astrophysics (grant 907524) and Astrobiology (grant 811073) Programs. A. M.

acknowledges the support of the National Research Council, and L. R. acknowledges the support of The SETI Institute Summer Research Experience for Undergraduates (funded by NSF award AST-0552751). The theoretical work by M. H.-G., T. J. L., and J. P. was supported through NASA's Astronomy and Physics Research and Analysis Program (APRA). As always, we are deeply indebted to Robert Walker for his outstanding technical support of all phases of the experimental work. We also gratefully acknowledge earlier insightful discussions with Jan Cami concerning the impact of the NIR transitions on the extinction curve.

## REFERENCES

- Allamandola, L. J., Tielens, A. G. G. M., & Barker, J. R. 1989, *ApJS*, 71, 733  
 Andrews, L., Friedman, R. S., & Kelsall, B. J. 1985, *J. Phys. Chem.*, 89, 4016  
 Appel, H., Gross, E. K. U., & Burke, K. 2003, *Phys. Rev. Lett.*, 90, 043005  
 Bakes, E. L. O., Tielens, A. G. G. M., & Bauschlicher, C. W. 2001, *ApJ*, 556, 501  
 Bauschlicher, C. W., & Langhoff, S. R. 1997, *Spectrochim. Acta Astron.*, 53, 1225  
 Becke, A. D. 1993, *J. Chem. Phys.*, 98, 5648  
 Bohlin, R. C., Savage, B. D., & Drake, J. F. 1978, *ApJ*, 224, 132  
 Bréchnignac, P., & Pino, T. 1999, *A&A*, 343, L49  
 Draine, B. T., & Li, A. 2001, *ApJ*, 551, 807  
 ———. 2007, *ApJ*, 657, 810  
 Dreuw, A., & Head-Gordon, M. 2005, *Chem. Rev.*, 105, 4009  
 Ehrenfreund, P., et al. 1995, *A&A*, 299, 213  
 Frisch, M. J., Pople, J. A., & Binkley, J. S. 1984, *J. Chem. Phys.*, 80, 3265  
 Halasinski, T., Weisman, J. L., Ruiterkamp, R., Lee, T. J., Salama, F., & Head-Gordon, M. J. 2003, *J. Phys. Chem.*, 107, 3660  
 Head-Gordon, M., Grana, A., Maurice, D., & White, C. 1995, *J. Phys. Chem.*, 99, 14261  
 Hertwig, R. H., & Koch, W. 1997, *Chem. Phys. Lett.*, 268, 345  
 Hirata, S., Head-Gordon, M., Szczepanski, J., & Vala, M. 2003, *J. Phys. Chem. A*, 107, 4940  
 Hirata, S., Lee, T. J., & Head-Gordon, M. 1999, *J. Chem. Phys.*, 111, 8904  
 Hudgins, D. M., & Allamandola, L. J. 1995a, *J. Phys. Chem.*, 99, 3033  
 ———. 1995b, *J. Phys. Chem.*, 99, 8978  
 ———. 2004, in *ASP Conf. Ser. 309, Astrophysics of Dust*, ed. A. N. Witt, G. C. Clayton, & B. T. Draine (San Francisco: ASP), 665  
 Hudgins, D. M., Bauschlicher, C. W., Jr., & Allamandola, L. J. 2001, *Spectrochim. Acta Astron.*, 57, 907  
 ———. 2005, *ApJ*, 632, 316  
 Hudgins, D. M., & Sandford, S. A. 1998, *J. Phys. Chem.*, 102, 329  
 Kjaergaard, H. G., Robinson, T. W., & Brooking, K. A. 2000, *J. Phys. Chem. A*, 104, 11297  
 Li, A., & Draine, B. T. 2001, *ApJ*, 554, 778  
 ———. 2002, *ApJ*, 572, 232  
 Mattila, K., et al. 1996, *A&A*, 315, L353  
 Mattioli, A. L., Hudgins, D. M., Bauschlicher, Jr., C. W., & Allamandola, L. J. 2005a, *Adv. Space Res.*, 36, 156  
 ———. 2005b, *ApJ*, 629, 1188  
 ———. 2005c, *ApJ*, 629, 1183  
 Mattioli, A. L., Hudgins, D. M., Bauschlicher, C. W., Jr., Rosi, M., & Allamandola, L. J. 2003, *J. Phys. Chem. A*, 107, 1486  
 Onaka, T., Yamamura, I., Tanabe, T., Roellig, T. L., & Yuen, L. 1996, *PASJ*, 48, L59  
 Pech, C., Joblin, C., Boissel, P. 2002, *A&A*, 388, 639  
 Peeters, E., Allamandola, L. J., Hudgins, D. M., Hony, S., & Tielens, A. G. G. M. 2004, in *ASP Conf. Ser. 309, Astrophysics of Dust*, ed. A. N. Witt, G. C. Clayton, & B. T. Draine (San Francisco: ASP), 141  
 Peeters, E., Hony, S., Van Kerkhoven, C., Tielens, A. G. G. M., Allamandola, L. J., Hudgins, D. M., & Bauschlicher, C. W. 2002, *A&A*, 390, 1089  
 Puget, J. L., & Leger, A. 1989, *ARA&A*, 27, 161  
 Salama, F., & Allamandola, L. J. 1991, *J. Chim. Phys.*, 94, 6964  
 Salama, F., Joblin, C., & Allamandola, L. J. 1994, *J. Chem. Phys.*, 101, 10252  
 Shao, Y., et al. 2006, *Phys. Chem. Chem. Phys.*, 8, 3172  
 Szczepanski, J., Banisaukas, J., Vala, M., Hirata, S., & Wiley, W. R. 2002, *J. Phys. Chem. A*, 106, 6935  
 Szczepanski, J., Vala, M., Dahbia, T., & Ellinger, Y., J. 1993, *Chem. Phys.*, 98, 4494  
 Vala, M., Szczepanski, J., Pauzat, F., Parisel, O., Talbi, D., & Ellinger, Y. 1994, *J. Phys. Chem.*, 98, 9187  
 Van Dishoeck, E. F. 2004, *ARA&A*, 42, 119  
 Verstraete, L., Pech, C., Moutou, C., Sellgren, K., Wright, C. M., Giard, M., Leger, A., Timmerman, R., & Drapatz, S. 2001, *A&A*, 372, 981  
 Zdzetsis, A. D., Garoufalidis, C. S., Grimme, S. 2001, *Phys. Rev. Lett.*, 87, 276402